

# Design of CMOS-MEMS broadband infrared emitter arrays integrated with metamaterial absorbers based on CMOS back-end-of-line

Zhengxi Cheng<sup>1,2</sup>, Hiroshi Toshiyoshi<sup>1</sup> ✉

<sup>1</sup>Research Center for Advanced Science and Technology, The University of Tokyo, Tokyo 153-8904, Japan

<sup>2</sup>Shanghai Institute of Technical Physics, Chinese Academy of Sciences, Shanghai 200083, People's Republic of China

✉ E-mail: hiro@iis.u-tokyo.ac.jp

Published in Micro & Nano Letters; Received on 13th May 2016; Revised on 15th July 2016; Accepted on 25th July 2016

A new design of complementary metal–oxide–semiconductor microelectromechanical systems (CMOS-MEMS) broadband infrared (IR) emitter arrays with integrated metamaterial absorbers (MAs) developed by the CMOS back-end-of-line is presented. The IR emitter array is a promising broadband thermal radiation source for integrated gas sensors. Novel IR emitter arrays are designed using the Central Semiconductor Manufacturing Corporation 0.5  $\mu\text{m}$  2-poly-3-metal CMOS process. To improve the low emissivity that is commonly seen in CMOS-MEMS type IR emitters due to the inherited low emissivity of  $\text{SiO}_2$  and  $\text{SiN}$  in CMOS process, we newly adopted tri-layer metal–insulator–metal (MIM) and four-layer insulator–MIM (IMIM) MA by using the CMOS back-end metal layers and inter-layer dielectrics, thereby to excite multi-mode surface plasmon polariton resonances. The emitter integrated with IMIM MA can be electrically modulated up to 344 Hz, as theoretically predicated from thermal properties of the emitters and the radiation properties calculated based on Planck's radiation law. Simulated emissivity spectra through FEM show that the multi-mode resonances in CMOS MIM and IMIM MAs enhance emissivity and broaden the waveband effectively.

**1. Introduction:** In this Letter, we report on complementary metal–oxide–semiconductor microelectromechanical systems infrared (CMOS-MEMS IR) emitter arrays based on our previous work [1] with more reliable process flow, broader waveband, and higher IR emissivity. Gas sensors based on IR absorption theories and photoacoustic theories are widely used in a series of applications, including health diagnosis, industrial processes monitoring, food safety inspection, and environmental monitoring, providing high sensitivity, fast response time, and excellent reliability [2]. Such IR gas sensors can simultaneously detect gas species and its concentration based on the unique IR absorption signature of gas molecule [3]. Broadband IR thermal radiation emitter with a waveband covering 1  $\mu\text{m}$  to 20  $\mu\text{m}$  is a key component for IR gas sensors [2].

CMOS MEMS IR emitters which take advantage of the standard CMOS fabrication technology to monolithically integrate read-in circuits and MEMS IR emitters, are promising low-cost micro broadband IR thermal radiation source for gas sensors. In many CMOS-MEMS IR emitters and similar micro-hot-plate applications [4], polysilicon resistors or tungsten resistors embedded in a  $\text{SiO}_2/\text{SiN}$  thin film stack were usually adopted as heating resistors. However, owing to the inherited low emissivity of  $\text{SiO}_2$  and  $\text{SiN}$  in the CMOS process, which are nearly transparent in short-wavelength and mid-wavelength IR waveband, this type of IR emitters commonly has a low radiance even at a high physical temperature, resulting in inefficient power dissipation, which is intensively concerned in portable applications.

Metamaterial absorber (MA) is an electromagnetic wave absorber which possesses absorption properties almost independent of the absorption properties of natural materials but mainly determined by the nanometric structural dimensions, and it can be artificially designed to have a near unity absorbance at specific wavelength even through the materials that have very weak IR absorption in that wavelength [5]. According to Kirchhoff's law, the emissivity of IR emitters equates with its absorbance. Thus, to enhance the emissivity of CMOS-MEMS IR emitters, especially in 2–5  $\mu\text{m}$  waveband in which  $\text{SiO}_2$  has an ignorable emissivity, tri-layer metal–insulator–metal (MIM) and four-layer insulator–MIM (IMIM) MAs consisted of metal and insulator layers are integrated

on the top of the CMOS-MEMS IR emitters by using the back-end-of-line (BEOL) of the standard CMOS process. The broadband MAs are made up of different absorber patterns assembled in the horizontal [6] or vertical [7] direction, and hence each pattern has its signature resonance mode; a complex absorbance pattern is also understood as a superposition of many peaks associated to single resonance modes [8]. By contrast, CMOS MIM MAs and IMIM MAs with thick dielectrics in CMOS process possess multiple resonance modes of surface plasmon polariton in the MIM cavities [9, 10], therefore it forms broadband absorbers, which improve the radiation efficiency of common IR emitters.

In this Letter, we present primary designs of  $8 \times 8$  scale CMOS MEMS broadband IR emitter arrays integrated with CMOS MAs. Tri-layer MIM and four-layer IMIM MA with multiple resonance modes are adopted to broaden and enhance the emitter IR emissivity. Trade-offs between power and speed, and between performance and releasing yield are compared in three different shapes of device designs. Read-in circuit was also integrated within each pixel of  $8 \times 8$  scale emitter array. A feasible post-CMOS MEMS process is proposed. The thermal properties of IR emitters are simulated by using finite-element method, and the radiation properties are also theoretically estimated based on Planck's radiation law. IR absorption spectra of the emitters are simulated by a commercial simulation tool COMSOL.

**2. Device geometries:** In each emitter, a micro plate suspended by narrow and long legs is used to attain excellent thermal isolation property. A serpentine-shape polysilicon resistor embedded in each emitter forms a heating resistor. Three different shapes of IR emitter are designed with trade-offs between power, temperature, response time, and thermal stress induced bending [11–13], as schematically shown in Fig. 1; details have been reported elsewhere [14]. Different from the standard design of type-I, an additional polysilicon line marked in the green square in type-II micro emitter is adopted as a heat spreader to make uniform temperature distribution on the micro emitter, as the thermal conductivity of polysilicon is higher than that of silicon dioxide.

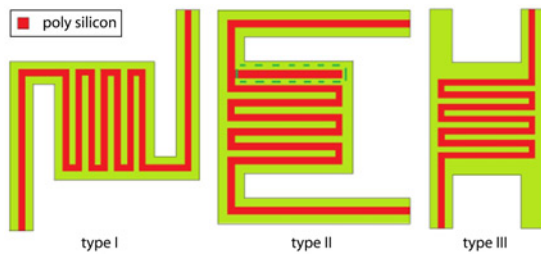


Fig. 1 Three shapes emitters

In all designs, the micro plate is commonly set to be  $20 \times 20 \mu\text{m}$  size, and the legs are  $5 \mu\text{m}$  wide.

To enhance the emissivity, IMIM-MAs and MIM-MAs developed by the CMOS BEOL are integrated on the top of the micro emitters. The cross-section view of the IR emitters is schematically shown in Fig. 2, along with a common CMOS-MEMS IR emitter with a poly silicon resistor embedded in the field oxide (FOX) and the inter-layer dielectrics (ILD) for reference. The typical sheet resistance of polysilicon (P1) is  $20 \Omega/\text{square}$ . IMIM-MAs consisted of a continuous layer of metal-1, inter-metal dielectric layer 1 (IMD1), metal-2 periodic square array, and IMD2, while MIM-MAs consisted of metal-1, IMD1 and metal-2. The width of metal-2 squares is  $0.7 \mu\text{m}$ , and the period of the array is  $1.4 \mu\text{m}$ .

An  $8 \times 8$  scale emitter array integrated with a read-in circuit, of which the X- and Y-direction scanning circuit are composed of an 8-bit D-type quasi-static shift register, is designed and fabricated by using the Central Semiconductor Manufacturing Corporation (CSMC)  $0.5 \mu\text{m}$  2-poly-3-metal CMOS process. In each pixel, a heating resistor is driven by an N-type metal-oxide-semiconductor transistor in a common source configuration, and a sample-and-hold circuit is used to maintain the gate voltage of the driver transistor, thereby keeping the thermal radiation stably without flicker. The fabricated chip and three different shapes emitters after the CMOS process are shown in Fig. 3.

**3. Post-CMOS process:** After the CMOS process, silicon wafers are post-CMOS processed as shown in Fig. 4. Both the emitters integrated with IMIM-MAs and that without MAs are simultaneously developed by the same process. The basic process flow is as follows. The Al pads are covered by Ti/Pt thin films by lift-off to avoid damage during wet etching in the following Al hard mask etching and bulk Si wet etching (Al pads and Ti/Pt layers are not shown here for clearance) (Fig. 4a). A hard mask for multi-layer dielectrics dry etching is patterned with sputtered Ti/Al thin films (Fig. 4b). The micro emitters are patterned by dry etching of dielectric layers to expose the silicon substrate (Fig. 4c). Removal of the aluminium hard mask by wet etching (Fig. 4d). Release of the micro emitters by the bulk silicon wet etching (Fig. 4e). The emitters integrated with MIM-MAs are obtained by time-control reactive ion etching (RIE) of IMD2 on the top of the emitters integrated with IMIM-MAs.

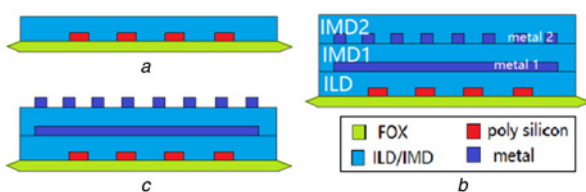


Fig. 2 Thin film stacks of micro emitters  
a Tri-layer stack of common emitter  
b Emitter integrated with IMIM MA  
c Emitter integrated with MIM MA

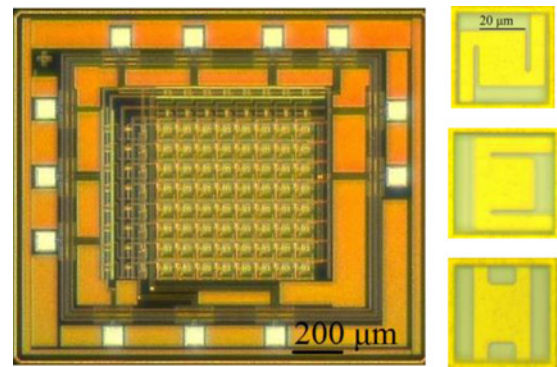


Fig. 3 Photographs of IR emitter array after CMOS process

Metal-1 is the hard mask in both the legs and the micro plane areas in common emitters during dielectrics dry etching, while metal-3 is the hard mask in the micro plane area and metal 2 in the legs area in the emitters integrated with IMIM MAs. In Fig. 4c, the metal-1/via/metal-2/via/metal-3 stacks in dashed squares are the sidewall protectors around the etched area, acting as a lateral hard mask during the etching of  $3\text{--}4 \mu\text{m}$  thick multi-layer dielectrics, to limit the lateral etching to an acceptable scale. To shorten the dry etching time, the thin gate oxide ( $125 \text{ \AA}$ ) substitutes the FOX ( $3800 \text{ \AA}$ ) in the release trench areas.

#### 4. Thermal properties simulations and radiation properties calculations:

The simulation and calculation process are described in detail elsewhere [14]. The physical temperature of each micro emitter under a constant biased voltage in steady-state has been simulated with COMSOL at a substrate temperature of  $273 \text{ K}$ . Thermal properties are adopted from [15, 16]. Since the IR emitters work in the vacuum package, we only take the thermal conduction through the supporting into the model. The

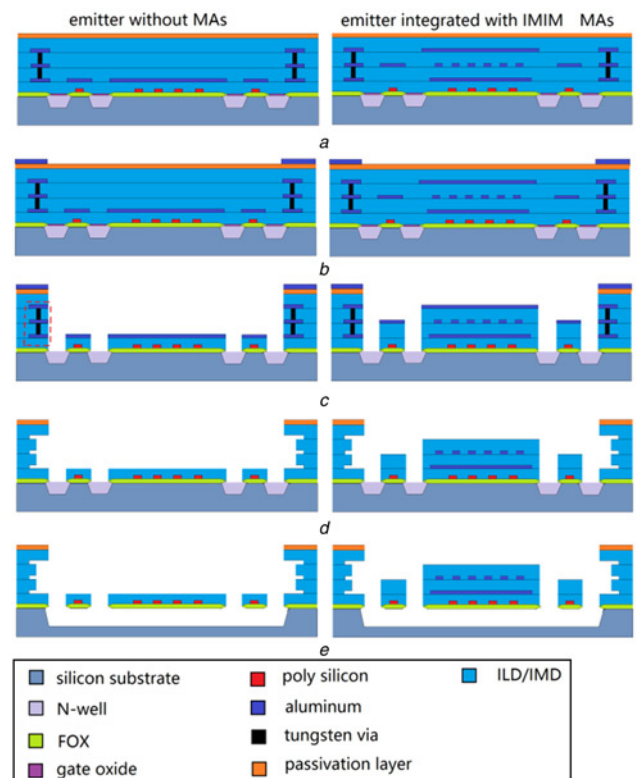
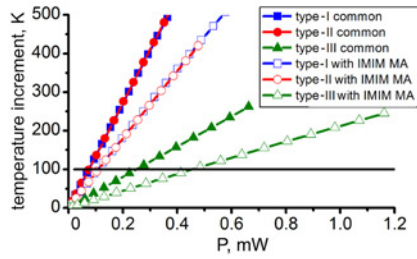
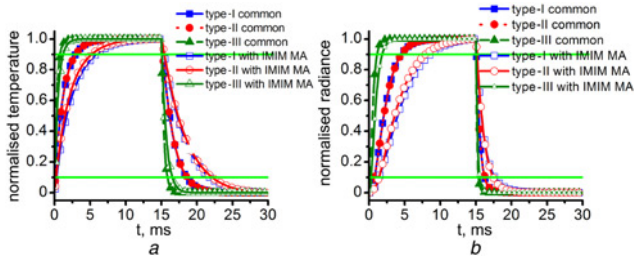


Fig. 4 Schematic diagram of post-CMOS process



**Fig. 5** Physical temperature–power relationship in steady state. 100 K line for reference



**Fig. 6** Dynamic responses of IR emitters. 0.1 and 0.9 lines for references  
a Thermal  
b Radiance

physical temperature – power relationship of each emitter in steady state is shown in Fig. 5, from which the thermal conductance  $G$  of each emitter is deduced, as

$$G = \frac{P}{\Delta T}, \quad (1)$$

where  $P$  is the power, and  $\Delta T$  is the temperature increment.

The emitters are also electrically biased with a square voltage of 10  $\mu$ s rise/fall time. The dynamic temperature responses are shown in Fig. 6a, in which the temperature is normalised to its maximum temperature increment. Thermal rise/fall time constants are the same ( $\tau_{\text{Trise}} = \tau_{\text{Tfall}}$ ) in the first-order approximation, ignoring the temperature dependence of material parameters. Thermal time constant  $\tau$  of each emitter is derived through the exponential fitting and listed in Table 1. With  $\tau$  and  $G$ , thermal mass  $C$  is calculated as

$$\tau = \frac{C}{G}. \quad (2)$$

Thermal mass  $C$  of each emitter is also listed in Table 1. Dynamic radiation responses are calculated based on the dynamic temperature responses through Planck's radiation law with a Matlab program. The normalised dynamic radiation response in the

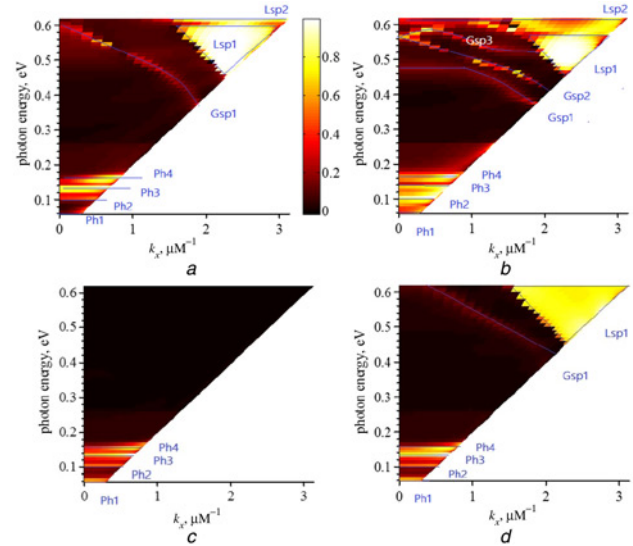


**Fig. 7** Angle-dependent absorbance spectra  
a MIM MAs, 0.55  $\mu$ m/0.8  $\mu$ m/0.55  $\mu$ m  
b IMIM MAs, 0.8  $\mu$ m/0.55  $\mu$ m/0.8  $\mu$ m/0.55  $\mu$ m  
c SiO<sub>2</sub> single-layer, 0.8  $\mu$ m  
d Al square array/SiO<sub>2</sub> layer, 0.55  $\mu$ m/0.8  $\mu$ m

waveband 3–5  $\mu$ m is shown in Fig. 6b. Radiance 10–90% rise time  $t_{\text{Rise}}$  and 90–10% fall time  $t_{\text{Fall}}$  are deduced, and listed in Table 1.

Although all emitters in the same group have quite a similar dimension of micro plate, type-III common emitter and type-III emitter with IMIM-MA have considerably larger thermal conductance compared with the other two emitters in the same group, and thus induced a relatively lower effective thermal mass. This effect enhances the operation speed of type-III common IR emitters and type-III emitter with IMIM-MA to 454 and 344 Hz, respectively, at the cost of a higher power consumption. Fig. 6a shows that the thermal rise time and fall time are quite close to each other. Fig. 6b depicts that the radiance rise time is longer than the thermal rise time, while the radiance fall time is shorter than the thermal fall time, which inherits from the relationship between temperature  $T$  and thermal radiance  $R$  that is  $R \propto T^4$ .

**5. Emissivity simulations:** IR absorption spectra of common IR emitters, IR emitter integrated with IMIM-Mas, and IR emitters integrated with MIM-MAs are simulated by COMSOL with aluminium and SiO<sub>2</sub> optical properties from [17, 18]. Due to the four-fold symmetrical geometry of the top metal squares and their array layout, the MAs are insensitive to the polarisation. Fig. 7 shows the simulated results of the transverse-magnetic-polarised angle-dependent absorbance spectra with the incident angle ranging from 0° to 87° with a pitch of 3°, in which  $k_x = 2\pi k \sin\theta$ , where  $k$  is the incident wave vector. For MIM MAs, four

**Table 1** Thermal properties and radiation properties of IR emitters

Emitters	Thermal conductance (10 <sup>−6</sup> W/K)	Thermal mass (10 <sup>−9</sup> J/K)	Thermal time constant, ms	Radiance rise time, ms	Radiance fall time, ms
type-I com	0.74	1.06	1.43	3.8	2.6
type-II com	0.74	1.07	1.45	3.8	2.6
type-III com	2.48	0.90	0.35	1.2	1.0
type-I w IMIM	1.10	3.11	2.82	8.3	2.4
type-II w IMIM	1.11	3.06	2.76	7.5	2.2
type-III w IMIM	4.54	2.74	0.60	1.6	1.3



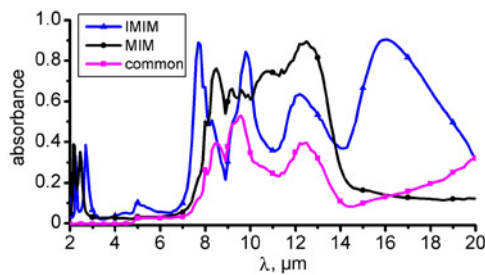


Fig. 8 Normal incidence IR absorption spectra of IR emitters

absorption peaks locates at 0.06, 0.1, 0.13, and 0.15 eV, marked as Ph1, Ph2, Ph3, and Ph4, respectively, in Fig. 7a, which are almost independent of incident angle, and form a wide absorption band. Ph1, Ph2, Ph3, and Ph4 correspond to the SiO<sub>2</sub> phonon absorption [19], which is verified by the SiO<sub>2</sub> thin film absorbance spectra in Fig 7c. The dispersion of the Gsp1 curve shows a grating-coupled surface plasmon polariton (GSPP) at the SiO<sub>2</sub>/Al or Air/Al interfaces [20]. The inverted triangle area labelled as Lsp1 between 0.46 and 0.59 eV and Lsp2 at 0.61 eV correspond to a series of Fabry–Perot type localised surface plasmon polaritons (LSPs) because of the multiple reflections between the upper and lower SiO<sub>2</sub> surfaces to form lateral standing waves in the square MIM cavities [9, 10]. Since the thickness of SiO<sub>2</sub> in the CMOS process is comparable with short IR wavelength, more standing-wave modes are accommodated in the square MIM cavities, thus CMOS MAs have more than one absorption peaks in the short-wavelength IR waveband, in contrast to the common monochrome MAs with a <100 nm thick dielectric layer which have only one main peak. Gsp1, Lsp1, and Lsp2 are consistent with those in Al square array/SiO<sub>2</sub> layer sample as shown in Fig. 7d. For IMIM MAs, more interfaces induce additional GSPP modes, thus show more absorption peaks in 0.46–0.62 eV, that is 2–2.7 μm waveband.

Normal incidence IR absorption spectra in Fig. 8 indicates that the common emitter has a negligible absorbance in 2–7 μm waveband, and has four absorption peaks at 8.5, 9.2, 12.6, and 20 μm wavelength, which are consistent with Ph1, Ph2, Ph3, and Ph4 in absorbance spectra in Fig. 7c. In contrast, the emitter integrated with IMIM-MA has two peaks of about 0.4 in 2–3 μm waveband, which come from the Lsp2 and Gsp2 (Gsp3) as shown in Fig. 7a. It also shows four separate absorption peaks with absorbance ranging from 0.7–0.9 in 7–20 μm waveband, which comes from the SiO<sub>2</sub> phonons absorption enhanced by the vertical multi-layer Fabry–Perot cavity. The emitters integrated with MIM-MA has two peaks about 0.4 in 2–3 μm from Gsp1 and Lsp2, and a SiO<sub>2</sub> phonons absorption band in 8–14 μm with absorbance ranging from 0.7–0.9.

**6. Conclusion:** CMOS-MEMS broadband IR emitter arrays integrated with MIM and IMIM MAs consisted of aluminium and silicon dioxide layers from CMOS BEOL and are designed by using the standard CSMC 0.5 μm 2P3M CMOS process. Simulated spectra show that multi-mode resonances, including GSPPs and LSPs, in MIM-MAs and IMIM-MAs enhance IR absorbance in 2–3 μm waveband, where SiO<sub>2</sub> is transparent and common CMOS-MEMS IR emitters have a very low emissivity. Besides that, the Fabry–Perot cavity of vertical multi-layer thin film stacks has an effect to enhance the emissivity in 7–14 μm waveband for both MAs and that in 14–20 μm waveband for IMIM-MAs. Thermal radiation simulation results show that type-III emitter with IMIM-MA function upwards of 344 Hz. The fast electrically modulated broadband CMOS-MEMS IR emitter

array is promising light source for IR gas sensors. Detail device performance is under investigation.

**7. Acknowledgments:** The author Zhengxi Cheng acknowledges the support of Youth Innovation Promotion Association CAS (grant no. 2013159) and the Program of Innovation Research in Shanghai Institute of Technical Physics (grant no. Q-ZY-86). The authors furthermore thank Kota Ito for his technical discussion.

## 8 References

- [1] Cheng Z., Toshiyoshi H.: 'Design of CMOS-MEMS infrared emitter arrays'. Proc. 11th Annual IEEE Int. Conf. on Nano/Micro Engineered and Molecular Systems (IEEE-NEMS 2016), Matsushima and Sendai, Japan, 17–20 April 2016
- [2] Konz W., Hildenbrand J., Bauersfeld M., ET AL.: 'Micromachined IR-source with excellent blackbody like behaviour'. Proc. of SPIE 5836, Sevilla, Spain, 1 July 2005, pp. 540–548
- [3] Hodgkinson J., Tatam R.P.: 'Optical gas sensing: a review', *Meas. Sci. Technol.*, 2012, **24**, (1), pp. 012004-1–012004-59
- [4] Mutinati G.C., Brunet E., Yurchenko O., ET AL.: 'Bimetallic nanoparticles for optimizing CMOS integrated SnO<sub>2</sub> gas sensor devices'. 44th European Solid State Device Research Conf. (ESSDERC), Venice, Italy, 2014, pp. 78–81
- [5] Hendrickson J., Guo J., Zhang B., ET AL.: 'Wideband perfect light absorber at midwave infrared using multiplexed metal structures', *Opt. Lett.*, 2012, **37**, (3), pp. 371–373
- [6] Liu X., Tyler T., Starr A.F., ET AL.: 'Taming the blackbody with infrared metamaterials as selective thermal emitters', *Phys. Rev. Lett.*, 2011, **107**, pp. 045901-1–045901-4
- [7] Ye Y.Q., Jin Y., He S.: 'Omnidirectional, polarization-insensitive and broadband thin absorber in the terahertz regime', *J. Opt. Soc. Am. B*, 2010, **27**, (3), pp. 498–504
- [8] Bossard J.A., Lin L., Yun S., ET AL.: 'Near-ideal optical metamaterial absorbers with super-octave bandwidth', *ACS Nano*, 2014, **8**, (2), pp. 1517–1524
- [9] Peng X.-Y., Wang B., Lai S., ET AL.: 'Ultrathin multi-band planar metamaterial absorber based on standing wave resonances', *Opt. Express*, 2012, **20**, (5), pp. 27756–27765
- [10] Nath J.: 'Selective electro-magnetic absorbers based on metal-dielectric-metal thin-film cavities', PhD dissertation, the University of Central Florida, Orlando, Florida, 2015
- [11] Cole B.E., Han C.J., Werner T.R., ET AL.: 'Ultra-low-power scene projector for targets against space backgrounds'. Proc. of SPIE, Orlando, USA, 1993, vol. 1967, pp. 39–50
- [12] Hsieh H.-S., Chang H.-C., Hu C.-F., ET AL.: 'A novel stress isolation guard-ring design for the improvement of a three-axis piezoresistive accelerometer', *J. Micromech. Microeng.*, 2011, **21**, (10), pp. 105006-1–105006-11
- [13] Sun Y.-C., Liang K.-C., Cheng C.-L., ET AL.: 'A CMOS MEMS pirani vacuum gauge with complementary bump heat sink and cavity heater'. Proc. of MEMS, San Francisco, USA, 2014, pp. 676–679
- [14] Cheng Z., Toshiyoshi H.: 'A design of integrated CMOS-MEMS infrared emitter arrays', *IEICE Electron. Express*, 2016, **13**, (7), pp. 1–10
- [15] Cole B.E., Han C.J., Higashi R.E., ET AL.: 'Monolithic 512 × 512 CMOS microbridge arrays for infrared scene projection'. The Eighth Int. Conf. on Solid State Sensors and Actuators, and Eurosensors IX, Sweden, 1995, pp. 628–631
- [16] Von Arx M., Paul O., Baltes H.: 'Process-dependent thin-film thermal conductivities for thermal CMOS MEMS', *J. Microelectromech. Syst.*, 2000, **9**, (1), pp. 136–145
- [17] Kitamura R., Pilon L., Jonasz M.: 'Optical constant of silica glass from extreme ultraviolet to far infrared at near room temperature', *Appl. Opt.*, 2007, **46**, (33), pp. 8118–8133
- [18] Ordal M.A., Long L.L., Bell R.J., ET AL.: 'Optical properties of the metals Al, Co, Cu, Au, Fe, Pb, Ni, Pd, Pt, Ag, Ti, and W in the infrared and far infrared', *Appl. Opt.*, 1983, **22**, (7), pp. 1099–1119
- [19] Chang P.-E., Jiang Y.-W., Chen H.-H., ET AL.: 'Wavelength selective plasmonic thermal emitter by polarization utilizing Fabry–Perot type resonance', *Appl. Phys. Lett.*, 2011, **98**, pp. 073111-1–073111-3
- [20] Tsai C.-M., Chang Y.-C., Tsai M.-W., ET AL.: 'Reflection and emission properties of an infrared emitter', *Opt. Express*, 2007, **15**, (22), pp. 14673–14678